



# Dynamic microstructural evolution of an Al–Zn–Mg–Cu alloy (7075) during continuous heating and the influence on the viscoelastic response

Jose I. Rojas<sup>a,\*</sup>, Daniel Crespo<sup>b</sup>

<sup>a</sup> Department of Physics–Division of Aerospace Engineering and Center for Research in NanoEngineering, Universitat Politècnica de Catalunya, c/ Esteve Terradas 7, 08860 Castelldefels, Spain

<sup>b</sup> Department of Physics and Center for Research in NanoEngineering, Universitat Politècnica de Catalunya, c/ Esteve Terradas 7, 08860 Castelldefels, Spain

## ARTICLE INFO

### Keywords:

Aluminum alloys  
Microanalysis  
Aging  
Internal friction  
Phase transformation

## ABSTRACT

The microstructural evolution of an Al–Zn–Mg–Cu alloy under continuous heating over the temperature range of 298 to 648 K (25 to 375 °C) is characterized by focused ion beam-scanning electron microscopy, transmission electron microscopy, and atom probe tomography. The chemical composition, dimensions, number density, and volume fraction of precipitates are measured comprehensively. Quantitative measurements of Guinier-Preston zones volume fraction and  $\eta'/\eta$  phase volume fraction are correlated to the viscoelastic response of the Al–Zn–Mg–Cu alloy with temperature in the studied range. This provides valuable evidence indicating that observed variations in the viscoelastic behavior of the Al–Zn–Mg–Cu alloy may be associated with phase transformations involving Guinier-Preston zones and phases  $\eta'$  and  $\eta$ .

## 1. Introduction

The aluminum alloy (AA) 7075 is a key representative of the Al–Zn–Mg alloy family (or 7xxx series), belonging to the group of heat-treatable alloys. After proper age hardening treatments, these alloys feature excellent mechanical properties and are highly suitable for a number of industrial applications, especially in the aerospace sector and transport industry [1]. Age hardening is based on the formation of precipitates from the decomposition of a metastable super-saturated solid solution, obtained by solution treatment and quenching. Precipitate-dislocation interaction is the main mechanism responsible for the hardening in these alloys [1]. The aging path and phase transformations, which depend on the alloy composition, quenching conditions and aging parameters (i.e., temperature and time), determine the microstructure (i.e., the precipitate morphology), and hence the material properties [1,2].

Much research has been devoted to investigating the aging paths of heat-treatable aluminum alloys [3]. For Al–Zn–Mg alloys, age-hardening is based essentially on the following aging path [2,4–7]: super-saturated solid solution – Guinier-Preston (GP) zones (I, II) –  $\eta'$  –  $\eta$ ; where GP zones are solute-rich coherent clusters,  $\eta'$  is the semi-coherent metastable hexagonal phase, and  $\eta$  is the incoherent stable (equilib-

rium) hexagonal phase. In Al–Zn–Mg–Cu alloys, a sequence based on phase T [6,8,9] and another based on phase S may also be present [10]. GP-I zones are Zn/Mg solute-rich coherent clusters internally ordered on {100} aluminum matrix planes, while GP-II zones are thin (a few atoms thick) Zn-enriched layers ordered on {111} planes [4,11,12]. GP-I zones are usually regarded as spherical, but researchers also report that they may appear slightly elongated [13] and that addition of Cu to Al–Zn–Mg alloys causes some GP zones to change from spherical to ellipsoidal shape [14]. Their diameter is of a few nm [2,4,11,14–18]. The  $\eta'$  particles are generally regarded as platelets [4,19] with size in the range 4–25 nm [4,11,16,19], while  $\eta$  particles are reported as either platelets [8,19] or rods [4,8], with similar size to  $\eta'$  particles [4,19]. Although the generally accepted equilibrium composition is  $\text{MgZn}_2$ , a more recent model suggests that the  $\eta'$  phase composition is  $\text{Mg}_2\text{Zn}_{(5-x)}\text{Al}_{(2+x)}$  [4,20]. The compositions reported for these phases are shown in Section 4.

For GP zones, number densities of  $1.5 \times 10^6$  [13,21] and  $3 \times 10^6$  GP zones per  $\mu\text{m}^3$  [8] were reported, and a volume fraction of 4% [8] and 2–6% [22]. In AA 7108, overall number densities from  $10^6$  to  $3 \times 10^6$  precipitates per  $\mu\text{m}^3$  were measured [4,11]. In AA 7136, a mixture of GP zones and  $\eta'$  phase was reported with a number density of  $2 \times 10^6$  precipitates per  $\mu\text{m}^3$  [23]. A volume fraction of 1–5% was reported for  $\eta'$  phase [22], while no volume fraction data were found for

\* Corresponding author.

Email addresses: [josep.ignasi.rojas@upc.edu](mailto:josep.ignasi.rojas@upc.edu) (J.I. Rojas); [daniel.crespo@upc.edu](mailto:daniel.crespo@upc.edu) (D. Crespo)

$\eta$  phase. Singh et al. [7] reported precipitates with an average maximum Feret diameter of 131.26 nm and volume fraction of 2.4%. However, from an engineering point of view, there is a gap between this knowledge and the most interesting macroscopic features, e.g., the mechanical behavior. Namely, there is a lack of theoretical models able to accurately correlate the microstructures with the viscoelastic properties of Al alloys.

While evidence on both the aging path and precipitate features comes mainly from microscopy analysis [20], the activation energies associated with transformations are generally obtained from calorimetric measurements [16]. However, experimental data in the literature are scattered and sometimes contradictory. This research aims to obtain coherent experimental information on the aging path, and the precipitate morphology and volume fraction under continuous heating at a constant heating rate, by complementary experimental techniques, including focused ion beam (FIB)-scanning electron microscopy (SEM), transmission electron microscopy (TEM), high-resolution TEM (HRTEM), and atom probe tomography (APT). This will provide essential experimental data to test a kinetic model for the viscoelastic response of AA 7075-T6 (Al-Zn-Mg-Cu alloy) over a variety of microstructures [24]. This way, observed variations in the viscoelastic behavior of the Al-Zn-Mg-Cu alloy can be correlated to the successive microstructural transformations.

## 2. Materials and Methods

The tested specimens were prepared from 2 mm thick sheet of commercial AA 7075-T6. The T6 temper consists of a solution heat-treatment at 753 K (480 °C) for 1 h, followed by rapid water quenching to room temperature (RT) and artificial aging at 393 K (120 °C) for 24 h. Tables 1 and 2 show, respectively, the mechanical properties and compositions in wt% and at.% for the as-received AA 7075-T6, as provided by the supplier (Alu-Stock, S.A.). Table 3 shows the particular treatment for each of the studied specimen types.

For TEM specimen preparation, plates were mechanically thinned down to 0.1 mm, and disks having 3 mm in diameter were punched out from these plates. The disks were electropolished in a one-step procedure, using a twin-jet Tenupol with an electrolyte of 25 vol% nitric acid in methanol [13], at 12 V and 251 K (− 22 °C). The TEM/HRTEM analysis was performed using a JEOL 3000F microscope, operated at 300 kV. The images are bright-field images obtained under two-beam conditions. A FIB-SEM Zeiss Neon40 was used to mill micron scaled trench structures in the specimens, producing cross-sectional views that were analyzed with secondary electron SEM. The FIB uses a column CANION31 of Ga, operated at 30 kV and 10 pA. The SEM uses a column GEMINI based on Schottky field emission, operated at extra high tension 2–5 kV, and uses ultra-high backscattered electrons (BSE) imaging. To verify the significance and consistency of the results, for SEM, an area of at least 16  $\mu\text{m}^2$  (the area of three images at the maxi-

mum SEM magnification used in this work) was analyzed for each specimen type; for TEM, an area of at least 1.6  $\mu\text{m}^2$  (the area of five images at the maximum TEM magnification used in this work); and for HRTEM, an area of at least  $8.1 \times 10^{-3} \mu\text{m}^2$  (the area of five images at the maximum HRTEM magnification used in this work). Namely, the area fraction values provided are the average from at least three SEM images. Precipitate boundaries were determined manually, based on image contrast. The high precipitate number density allowed performing random area analysis [8].

For atom probe, thin bars were prepared with 20 mm in length and  $0.5 \times 0.5 \text{ mm}^2$  square cross-section. The bars were subjected to a two-step electro-polishing procedure to obtain the final needle shape [13,25]. The first step uses an electrolyte of 25 vol% perchloric acid in acetic acid at 20 V at RT. The second step (a finer electropolishing under the light microscope) uses an electrolyte of 5 vol% (initially) and 2 vol% (finally) perchloric acid in 2-butoxyethanol at 23 V at RT. Atom probe microscopy was performed on an IMAGO LEAP 3000Si atom probe at a base specimen temperature of 39 K, a pulse fraction of 20% DC voltage, a pulsing rate of  $2 \times 10^5$  Hz and a target evaporation rate of 0.50% in the ultra-high vacuum of  $< 3 \times 10^{-11}$  Torr. The ion flight distance was 90 mm, and the detector efficiency of the instrument is 57% [26]. The reconstruction and data analysis were performed using the software IVAS 3.6.4. In each data set, at least  $1 \times 10^6$  ions were collected and up to three data sets were analyzed for each condition. Iso-concentration surfaces were used to identify solute-enriched regions in the analyzed volumes [27], with a threshold value of the combined Zn + Mg content set to 20 at.%, more than three times over the combined Zn + Mg content of the alloy. The concentration of Al, Cu, Mg, and Zn in the matrix was measured from selected volumes containing no precipitates or poles. The dimensions of these analysis cylinders and those used to obtain concentration profiles across precipitates were 10–20 nm long, 2.5–5 nm in radius. For all the quantitative results, the error bars represent one standard deviation on each of the average values. Finally, test data on the viscoelastic behavior of AA 7075-T6 were also used [24,28]. More details on the viscoelastic measurements and the dynamic-mechanical analyzer can be found in these works and as Supplementary material.

## 3. Results

### 3.1. Specimen 1: As-received AA 7075-T6

In the analyzed SEM images, contrast can be observed from a distribution of small and large particles brighter than the matrix (see Fig. 1). This indicates that their Zn content is high, as Zn atoms are heavier than Al atoms. A hexagonal character can be observed for some large particles. The identification of these particles as  $\eta'$  phase is discussed in-depth in the following sections, where TEM images and APT results are available. Presence of  $\eta'$  phase is expected in the as-received AA 7075-T6 due to the artificial aging of the T6 temper [5,16,29]. The  $\eta'$  phase area fraction is  $1.26 \pm 0.15\%$ . This result does not account for the small precipitates, as it is not possible to discriminate whether they are GP zones or  $\eta'$  particles, and it is hard to assure whether they are actually cut by the cutting face or they are just halos from precipitates in deeper layers. Nevertheless, the measured area fraction is considered

**Table 1**  
Mechanical properties of the as-received, commercial aluminum alloy (AA) 7075-T6.

Aluminum alloy	Yield stress	UTS	% area reduction	Brinell hardness
AA 7075-T6	502 MPa	583 MPa	12%	HB 161

**Table 2**  
Chemical composition of the as-received, commercial aluminum alloy (AA) 7075-T6.

Aluminum alloy	Units	Si	Fe	Cu	Mn	Mg	Zn	Ti	Cr	Al
AA 7075-T6	wt%	0.06	0.15	1.50	0.01	2.58	6.00	0.05	0.19	89.46
	at.%	0.06	0.08	0.67	0.01	2.99	2.59	0.03	0.10	93.48

**Table 3**  
Heat-treatment for each studied specimen.

Specimen #	Treatment	Heating temperature	Heating rate	Cooling
1	AA 7075-T6	As received	–	–
2	AA 7075-T6	383 K (110 °C)	1 K/min	Air quenched
3	AA 7075-T6	443 K (170 °C)	1 K/min	Air quenched
4	AA 7075-T6	503 K (230 °C)	1 K/min	Air quenched
5	AA 7075-T6	563 K (290 °C)	1 K/min	Air quenched
6	AA 7075-T6	648 K (375 °C)	1 K/min	Air quenched

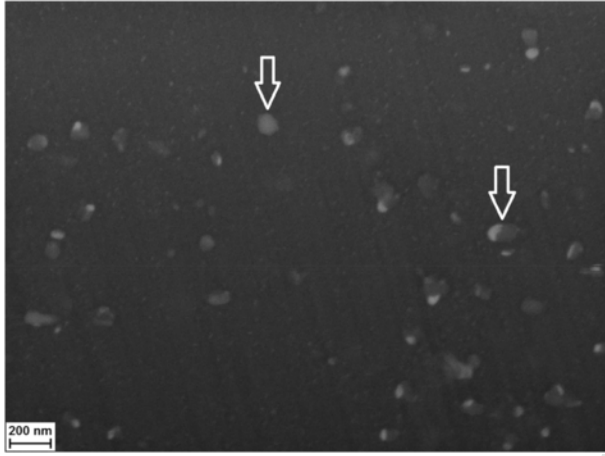


**Fig. 1.** SEM image for as-received AA 7075-T6. The particles marked with arrows show presumably the hexagonal character of  $\eta'$  cells, confirmed by TEM analysis of specimens 2 to 5.

accurate enough for the purpose of this research since the contribution of the small  $\eta'$  particles, if any, is very small. The volume fraction can be derived from SEM images because, for a 3D distribution of particles, it is equal to the area fraction measured in the cutting face of a random cut [30]. The parallel grooves observed in some SEM images are due to the FIB milling. Additional SEM images can be found for specimens 1 to 6 as Supplementary material.

### 3.2. Specimen 2: AA 7075-T6 Heated up to 383 K (110 °C)

Fig. 2 shows an atom map for the Al, Cu, Mg and Zn distributions, and iso-concentration surfaces for the Mg distribution. These are slightly smaller than the iso-concentration surfaces for the Zn distribution because diffusion of Zn is faster [2], and this affects the size of the surfaces especially at low temperatures, like 383 K (110 °C) (atom maps for the individual Cu, Mg and Zn distributions and iso-concentration surfaces for the Zn distribution can be found for specimens 2, 3 and 5 as Supplementary material). A fine dense uniform distribution of Zn/Mg solute-rich clusters can be observed. The clusters are spherical or ellipsoidal, with a number density of  $3.5 \pm 0.6 \times 10^6$  clusters per  $\mu\text{m}^3$ . This value is the average of three APT analyses. The average cluster characteristic length  $L$ , computed from two orthogonal lengths  $l_1$  and  $l_2$  for each cluster as  $L = \frac{1}{N} \sum_{i=1}^N \sqrt{l_1 l_2}$ , is  $4.2 \pm 1.2$  nm (average from over 20 clusters). Fig. 2 shows also Al, Cu, Mg and Zn concentration profiles across one cluster (additional concentration profiles can be found for specimens 2 and 3 as Supplementary material). Table 4 presents the Al, Cu, Mg and Zn concentration and the Zn:Mg ratio for the

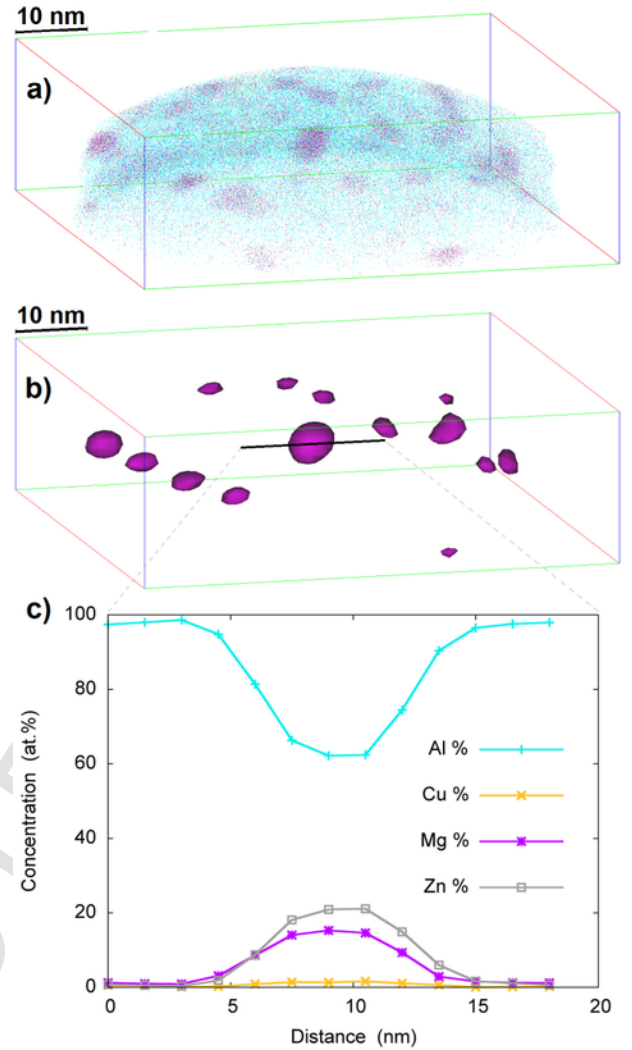


**Fig. 2.** For AA 7075-T6 heated up to 383 K (110 °C): a) Al, Cu, Mg and Zn atom map; b) volumes with 5 or more Mg atoms per  $\text{nm}^3$ ; c) 1D concentration profiles of Al, Cu, Mg and Zn in at.% across a GP zone, using an analysis cylinder with revolution symmetry axis centered along a diameter of the GP zone.

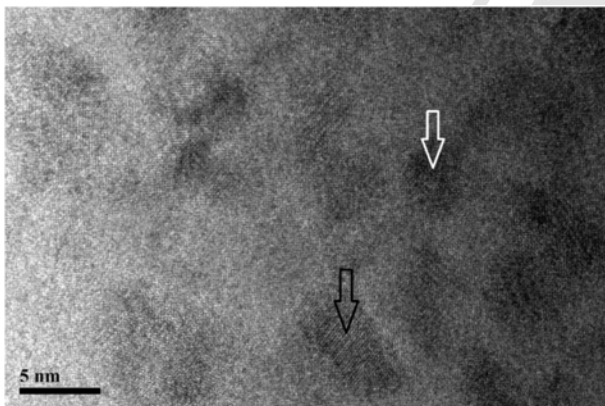
as-received alloy, and for the matrix and precipitates observed in specimens 2, 3 and 5, together with results from the literature. The measured cluster composition (in particular, the Zn:Mg ratio, the Cu content and the combined Zn/Mg content) compares well with values attributed to GP zones (see Table 4). The Zn:Mg ratio of GP-I zones and  $\eta'$  particles may be similar, but the overall composition is not necessarily the same, e.g., in  $\eta'$  particles the Al content is lower than in GP-I zones [13], as occurs in our results. Thus, based on their shape, size and composition, the clusters are preliminarily identified as GP-I zones.

Fig. 3 shows an HRTEM image from a  $\{110\}_{\text{Al}}$  zone axis. Contrast can be observed from a dense uniform distribution of fine clusters darker than the matrix. This indicates that their Zn content is high, as Zn atoms are heavier than Al atoms. No extra spots or diffuse scattering indicating the presence of precipitates are observed in the selected area diffraction (SAD) patterns, suggesting that the clusters are coherent. From their 2D sections, the clusters can be regarded as spherical or ellipsoidal. The average value of  $L$  for the clusters, as obtained from the HRTEM images, is shown in Section 4 (additional HRTEM images can be found for specimens 2 and 3 as Supplementary material). These findings confirm the previous identification of the clusters as GP-I zones from APT. Lower magnification TEM images from a  $\{110\}_{\text{Al}}$  zone axis were analyzed, which is very appropriate as the  $c$ -axis of the

**Table 4**

Al, Cu, Mg and Zn concentration, and Zn:Mg ratio, in at.%, of the as-received alloy, and the matrix and observed phases in AA 7075-T6 heated up to 383, 443 and 563 K (110, 170 and 290 °C), compared with results in the literature from previous studies of related alloys. Stacked histograms can be found in the Supplementary material.

Concept	Al (at.%)	Cu (at.%)	Mg (at.%)	Zn (at.%)	Zn:Mg
As-received alloy	93.48	0.67	2.99	2.59	0.86
Matrix, 383 K (110 °C)	97.21 ± 0.63	0.46 ± 0.14	1.56 ± 0.26	0.75 ± 0.33	–
Matrix, 443 K (170 °C)	98.80 ± 0.28	0.12 ± 0.08	0.57 ± 0.12	0.50 ± 0.15	–
Matrix, 563 K (290 °C)	97.74 ± 0.34	0.15 ± 0.05	0.56 ± 0.12	0.83 ± 0.20	–
Matrix in AA 7150 [8]	94.9 ± 0.3	0.8 ± 0.1	2.2 ± 0.2	2.1 ± 0.2	–
Matrix in AA 7108-T6 [35]	98.36 ± 0.13	–	0.30 ± 0.06	1.34 ± 0.12	–
Matrix in AA 7108-T7 [35]	98.81 ± 0.05	–	0.17 ± 0.02	1.02 ± 0.05	–
Matrix in AA 7050 [13]	–	0.75	2.00	1.50	–
Matrix [18]	98.89 ± 0.05	–	0.50 ± 0.03	0.62 ± 0.04	–
Matrix in AA 7050 [36]	96.0 ± 0.3	0.7 ± 0.02	1.8 ± 0.2	1.5 ± 0.2	–
GP-I zones, 383 K (110 °C)	67.75 ± 10.61	1.23 ± 0.33	13.80 ± 5.02	17.04 ± 5.55	1.27 ± 0.20
GP-I zones, 443 K (170 °C)	69.68 ± 6.97	4.92 ± 1.32	13.78 ± 2.67	11.35 ± 3.22	0.81 ± 0.13
GP-I zones, 563 K (290 °C)	Not found	Not found	Not found	Not found	Not found
GP zones [6]	–	–	6	9	1.4
GP zones in AA 7150 [8]	68 ± 8	2 ± 2	13 ± 6	17 ± 6	1.31
GP zones [15]	–	–	20	20	1
GP zones [12]	–	1–3	15–20	20–25	1.3
GP zones in AA 7050 [13]	–	12 ± 2; 8 ± 1	47 ± 4; 46 ± 2	40 ± 4; 46 ± 2	0.85; 1; 1.2
GP zones [14]	–	0–1.1	5.8–16.4	7.4–18.1	0.89–1.55
GP zones in AA 7050 [36]	67 ± 5	0.9 ± 0.3	14 ± 2	18 ± 3	1.3 ± 0.1
η' phase, 383 K (110 °C)	Not found	Not found	Not found	Not found	Not found
η' phase, 443 K (170 °C)	64.89 ± 5.33	5.18 ± 1.02	15.71 ± 2.14	14.03 ± 2.37	0.89 ± 0.07
η' phase, 563 K (290 °C)	Not found	Not found	Not found	Not found	Not found
η' phase [6]	–	–	11; 27	13; 39	1.2; 1.4
η' phase in AA 7050 [9]	–	2; 3	20; 16.5	24; 22	1.2; 1.3
η' phase [18]	61.38 ± 5.02	–	19.38 ± 2.45	19.25 ± 2.73	1.01 ± 0.03
η' phase in AA 7050 [13]	–	11 ± 2; 5 ± 1	42 ± 3; 42 ± 1	46 ± 3; 53 ± 1	1.09; 1.26
η' phase [36]	70.4 ± 7.0	4.0 ± 0.7	14.9 ± 6.8	10.5 ± 3.1	0.7 ± 0.1
η phase, 383 K (110 °C)	Not found	Not found	Not found	Not found	Not found
η phase, 443 K (170 °C)	Not found	Not found	Not found	Not found	Not found
η phase, 563 K (290 °C)	50.89 ± 2.86	0.61 ± 0.17	23.83 ± 2.62	23.21 ± 1.26	0.98 ± 0.10
η phase [6]	–	–	17	36	2.1
η phase in AA 7050 [9]	–	8	25	26	1
η phase in AA 7108-T6 [35]	30.64 ± 2.47	–	25.17 ± 1.61	44.19 ± 1.84	1.76
η phase in AA 7108-T7 [35]	8.45 ± 0.94	–	32.46 ± 0.79	59.05 ± 0.83	1.82
η phase [18]	48.18 ± 8.85	–	24.00 ± 5.31	27.73 ± 4.51	1.18 ± 0.21
η phase in AA 7136 [23]	7.4 ± 0.1	8.6 ± 0.1	38.6 ± 0.4	45.4 ± 0.5	1.18
η phase [36]	58 ± 9	2.4 ± 0.4	18 ± 2	22 ± 5	1.2 ± 0.1



**Fig. 3.** Bright-field HRTEM image from a  $\langle 110 \rangle_{\text{Al}}$  zone axis, for AA 7075-T6, heated up to 383 K (110 °C). Two GP zones, presumably spherical and ellipsoidal, are marked with a white and a black arrow, respectively.

hexagonal  $\eta'$  cells fit  $\{111\}$  matrix planes [4,20]. Precipitates with hexagonal character appear in all the images, while platelets are only observed in one image. In specimens 1 to 6, these particles are identified as phases of the  $\eta$ -based sequence for two reasons. First, the Cu content of the alloy is below 2.5 wt%, and thus Cu is not expected to form S phase, but to dissolve in the matrix or in phases of the  $\eta$ - and T-based sequences [31]. Second, phases T' and T show cubic character [6], not hexagonal, and their composition [6,8,32] is very different to that obtained for the platelets (see Table 4). For specimen 2, the tem-

perature range for  $\eta'$  (and of course  $\eta$ ) phase formation was not reached (a summary of transformation temperatures in the  $\eta$ -based sequence can be found in [24]). Hence, the observed platelet-shaped particles and hexagonal particles are identified as  $\eta'$  phase inherited from the microstructure of the as-received AA 7075-T6 (i.e., from primary precipitation during the artificial aging of the T6 temper). For specimens 2 to 5, the average  $a$ -edge length and  $c$ -axis length of the hexagonal cells are shown in Section 4. The  $a$ -edge length values provide only information on the order of magnitude since the hexagonal faces are not seen in true scale.

In the analyzed SEM images, the large particles high in Zn content are primary  $\eta'$  phase, as explained above. The small precipitates are probably the largest GP zones and small primary  $\eta'$  particles, but it is not possible to discriminate. The  $\eta'$  phase area fraction, providing a good estimation of the volume fraction [30], is  $1.25 \pm 0.06\%$ . Not surprisingly, this result is very similar to that for specimen 1, since formation of new (secondary)  $\eta'$  phase is not expected yet.

### 3.3. Specimen 3: AA 7075-T6 Heated up to 443 K (170 °C)

Fig. 4 shows an atom map for the Al, Cu, Mg and Zn distributions, and iso-concentration surfaces for the Mg distribution. A fine dense uniform distribution of Zn/Mg solute-rich clusters can be observed. The clusters are spherical or ellipsoidal, with  $L$  of  $4.6 \pm 1.4$  nm (average from over 20 clusters) and number density of  $1.6 \pm 0.0 \times 10^6$  clusters per  $\mu\text{m}^3$ . Platelet-shaped particles are also observed, with length and width around 7–10 nm, and thickness 4 nm, and number density of

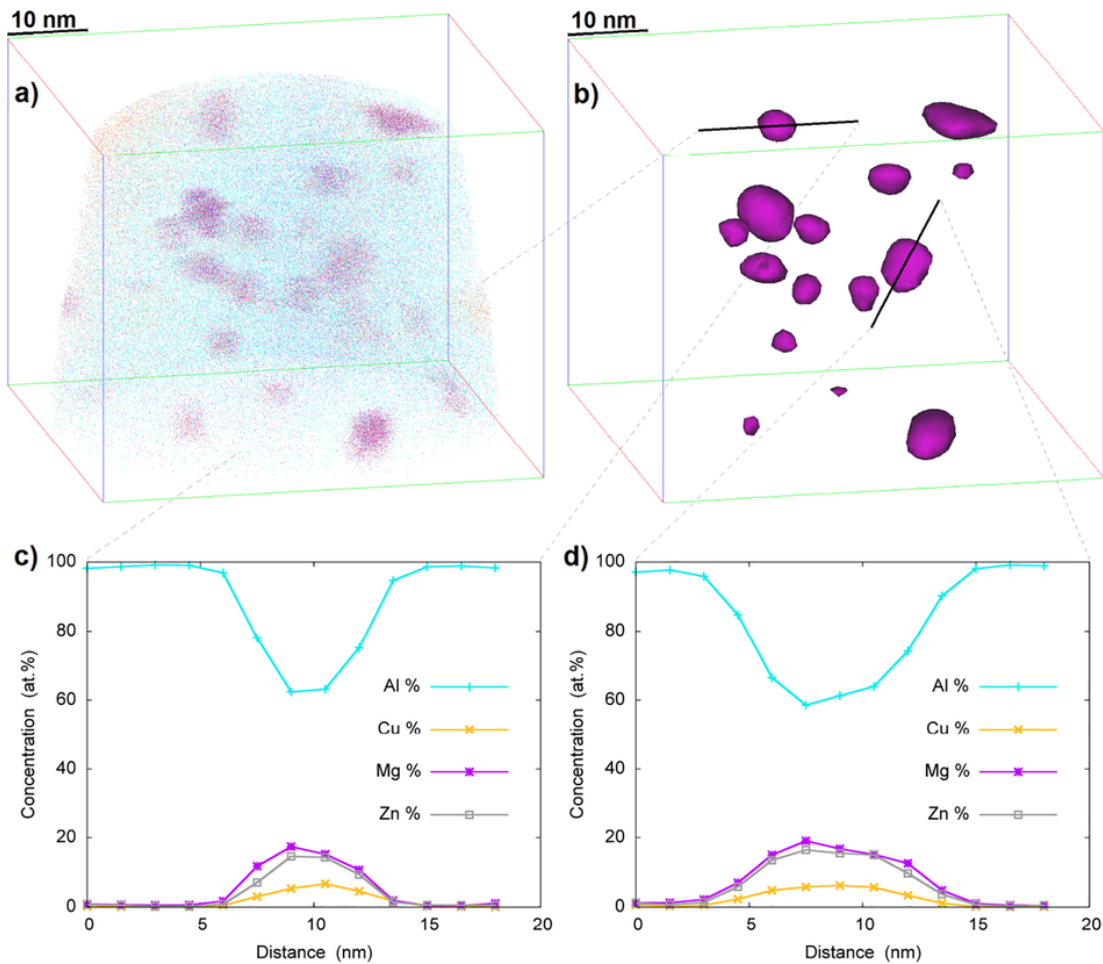


**Fig. 4.** For AA 7075-T6 heated up to 443 K (170 °C): a) Al, Cu, Mg and Zn atom map; b) volumes with 5 or more Mg atoms per nm<sup>3</sup>; 1D concentration profiles of Al, Cu, Mg and Zn in at.% across c) a GP zone, and d) an η' particle, using analysis cylinders with revolution symmetry axis centered along a diameter of the GP zone and along the η' particle habit plane, respectively (1D concentration profiles along a direction normal to the η' particle habit plane can be found as Supplementary material).

$5.1 \pm 1.3 \times 10^5$  platelets per μm<sup>3</sup>. The densities are the average from two APT analyses. Fig. 4 shows also Al, Cu, Mg and Zn concentration profiles across one cluster and one platelet. The measured compositions are shown in Table 4. Based on their shape, size, and composition, the clusters are preliminarily identified as GP-I zones.

It is more complicated to establish whether the platelets are η' or η particles. The composition compares well with that reported for η' phase (see Table 4), but it was suggested that, while the total amount of solute in η' particles is smaller than in η particles, the similarity of their Zn:Mg ratio does not allow discrimination based on this ratio only [4,18]. In another work [6], the composition of η' phase was closer to GP zones rather than the traditional equilibrium stoichiometry MgZn<sub>2</sub>, and the Zn:Mg ratio of the η' phase had a good 1:1 correlation with the Zn:Mg ratio of the as-received alloy. The same occurs in our results. Finally, it is expected that η' and η phases incorporate a substantial amount of Al [9,32], e.g., 55 and 40 at.% for η' phase and η phase, respectively [9]. For specimen 3, the minimum Al content of the platelets is 50–65 at.%. There is significant Cu solute segregation to the particles, but precipitates from the η-based sequence may dissolve considerable amounts of Cu in them [31]. Bearing in mind these considerations and those in previous sections, and based on the heat-treatment applied to specimen 3, the platelet is most probably η' phase. Particularly, η phase formation may only start above 493 K (220 °C) [5,16,33,34], while η' phase formation may start at 373 K (100 °C) [2].

Thus, the platelets are either inherited (primary) η' particles or newly formed (secondary) η' particles.

Fig. 5 shows an HRTEM image from a  $\bar{1}10_{\text{Al}}$  zone axis. A dense distribution of clusters is observed, which appear darker, indicating Zn-enrichment. The SAD patterns suggest that the clusters are fully coherent. The clusters are spherical or ellipsoidal, having larger dimensions than those observed for specimen 2 (see Section 4). These findings confirm the previous identification of the clusters as GP-I zones from APT.

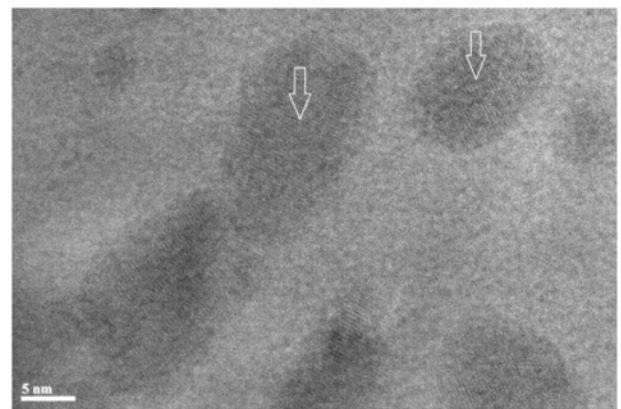


**Fig. 5.** Bright-field HRTEM image from a  $\bar{1}10_{\text{Al}}$  zone axis, for AA 7075-T6, heated up to 443 K (170 °C). Two GP zones, presumably ellipsoidal, are marked with arrows.



Lower magnification TEM images were analyzed. Some precipitates exhibit hexagonal character (see averaged dimensions in Section 4). In the analyzed SEM images, the large precipitates are primary  $\eta'$  particles. The small particles are probably the largest GP zones and small  $\eta'$  particles (primary or secondary), but it is not possible to discriminate. The  $\eta'$  phase area fraction is  $1.47 \pm 0.08\%$ .

### 3.4. Specimen 4: AA 7075-T6 Heated up to 503 K (230 °C)

Fig. 6 shows a TEM image from a  $\{110\}_{\text{Al}}$  zone axis. The particles are identified as  $\eta'$  phase because: 1) they are too large for being GP

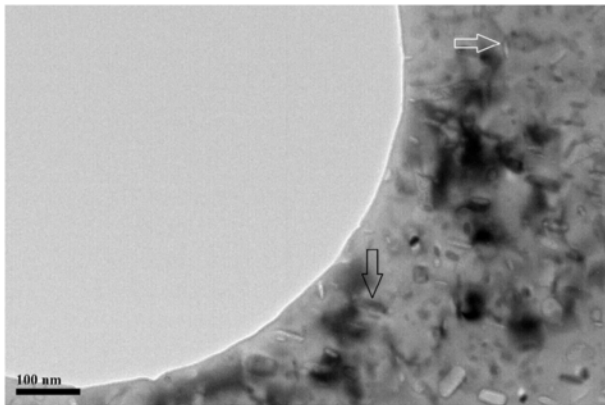


Fig. 6. Bright-field TEM image from a  $\{110\}_{\text{Al}}$  zone axis, for AA 7075-T6, heated up to 503 K (230 °C). A particle showing the hexagonal character of the  $\eta'$  cell is marked with a white arrow, and a particle with the c-axis in true scale is marked with a black arrow.

zones, 2) dissolution of GP zones should be completed at 493 K (220 °C) [16,29] or well below [5,33], and 3) particles with hexagonal character and particles with the c-axis in true scale can be observed (see Section 4). Indeed,  $\eta$  phase formation may start at 493 K (220 °C) [16,34] but, given the short time that specimen 4 was above 493 K (220 °C), the presence of  $\eta$  phase is assumed negligible. The  $\eta'$  phase area fraction measured in the SEM images (see Supplementary material) is  $1.87 \pm 0.17\%$ .

### 3.5. Specimen 5: AA 7075-T6 Heated up to 563 K (290 °C)

Fig. 7 shows atom maps for the Cu, Mg and Zn distributions, and iso-concentration surfaces for the Mg distribution. Half of a large platelet-shaped Zn/Mg solute-rich region can be observed, resulting in a number density of  $4.6 \times 10^4$  precipitates per  $\mu\text{m}^3$ , and volume fraction of 1.30%, but these values have an inherent large uncertainty. The part of the platelet inside the analyzed volume is around 10 nm long, 8.5 nm wide and 7 nm thick. Fig. 7 shows also Al, Cu, Mg and Zn concentration profiles across the particle. Notwithstanding the high dispersion in compositions of precipitates of the  $\eta$ -based sequence in the literature, the measured Mg and Zn content is higher than most of the compositions reported for  $\eta'$  phase and is comparable to compositions reported for  $\eta$  phase (see Table 4). Our results agree also with a higher total solute content reported for  $\eta$  particles respect to  $\eta'$  particles [4,18]. Bearing in mind these considerations and those in previous sections, and based on abundant research showing that  $\eta$  phase formation occurs between 493 and 579 K (220 and 306 °C) [5,16,33,34], the platelet is most probably  $\eta$  phase.

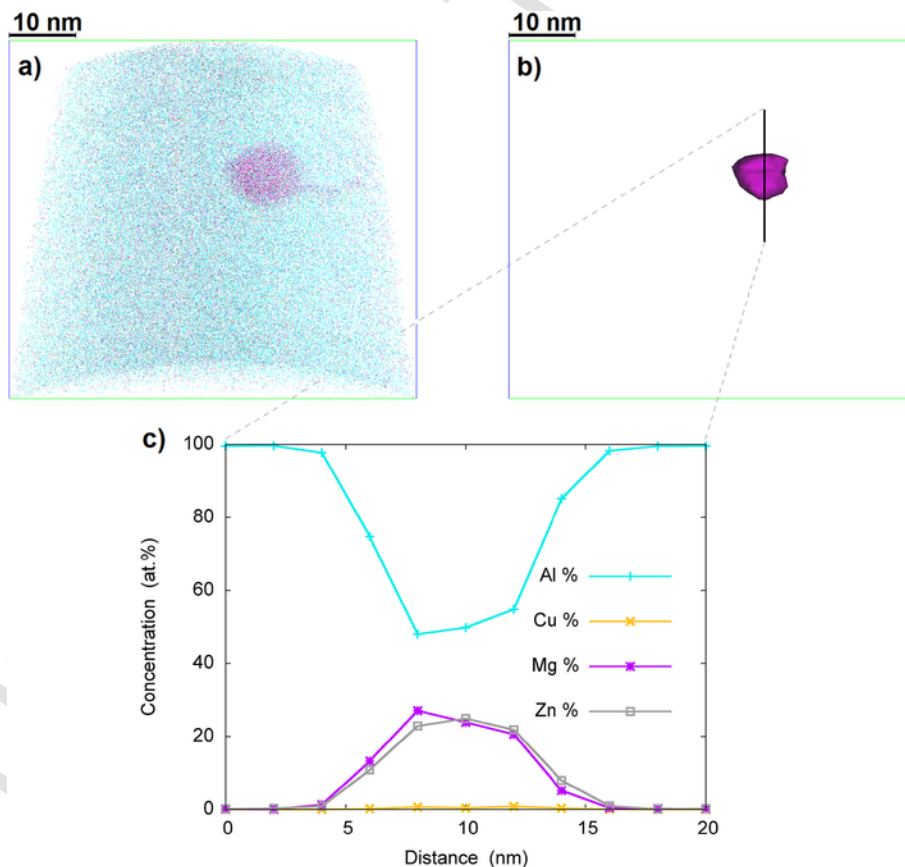


Fig. 7. For AA 7075-T6 heated up to 563 K (290 °C): a) Al, Cu, Mg and Zn atom map; b) volumes with 5 or more Mg atoms per  $\text{nm}^3$ ; c) 1D concentration profiles of Al, Cu, Mg and Zn in at.% across an  $\eta$  particle, using an analysis cylinder with revolution symmetry axis normal to the platelet habit plane.

Fig. 8 shows a TEM image from a  $\gamma\text{001}_{\text{Al}}$  zone axis. The hexagonal character of  $\eta'$  and  $\eta$  cells can be observed (see averaged dimensions in Section 4). It is not possible to differentiate all the  $\eta$  particles from the  $\eta'$  particles, though. In some cases, discrimination could be made based on the shape (some authors suggest that  $\eta$  phase may also be rod-shaped [4,8,18]), but most importantly based on their orientations, because the  $c$ -axis of  $\eta'$  cells fits to  $\{111\}$  planes [4,20], while  $\eta$  particles appear with different orientations respect to the matrix [18]. Namely, in TEM images from a  $\gamma\text{001}_{\text{Al}}$  zone axis, platelets with the  $c$ -axis in true scale cannot be  $\eta'$  phase and thus must be  $\eta$  phase (additional TEM images can be found for specimen 5 as Supplementary material). Particles were observed in the SEM images, which may be either  $\eta'$  or  $\eta$  phase. Due to the limitations in particle discrimination, the area fraction measured for specimen 5 ( $4.81 \pm 0.27\%$ ) is assumed to be that of the combined  $\eta'$  and  $\eta$  phases.

### 3.6. Specimen 6: AA 7075-T6 Heated up to 648 K (375 °C)

Fig. 9 shows an inverse contrast SEM image, where particles darker than the matrix are those high in Zn content, like in TEM images. Based on the temperature reached in the heating, at which presence of  $\eta'$  phase is unlikely, but considering also their shape and size, the particles are identified as  $\eta$  phase. In this case, the area fraction is  $5.48 \pm 0.00\%$ .

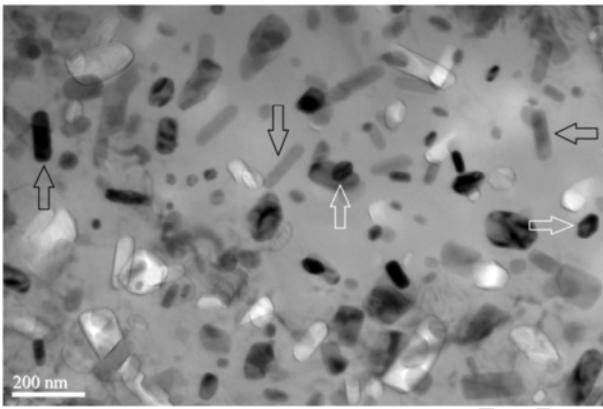


Fig. 8. Bright-field TEM image from a  $\gamma\text{001}_{\text{Al}}$  zone axis, for AA 7075-T6, heated up to 563 K (290 °C). Two particles showing the hexagonal character of  $\eta'$  and  $\eta$  cells are marked with white arrows. Three  $\eta$  particles with the  $c$ -axis in true scale are marked with black arrows.

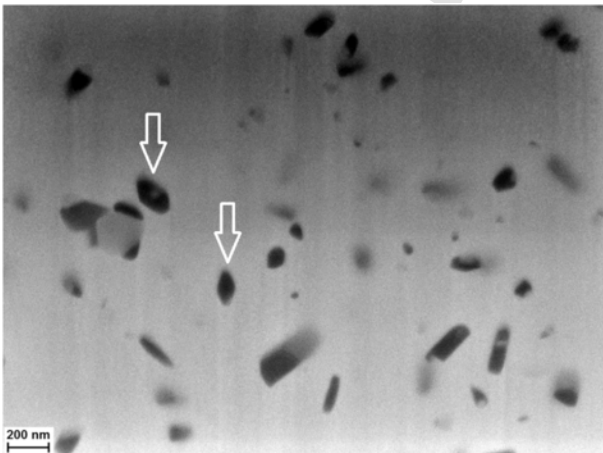


Fig. 9. Inverse contrast SEM image for AA 7075-T6 heated up to 648 K (375 °C). Two particles showing the hexagonal character of  $\eta$  cells are marked with arrows.

## 4. Discussion of Experimental Results

Table 4 shows measured chemical compositions and solute concentrations of the matrix and observed phases. For the phases, each data point represents the average from 3 to 9 sections (1.5 nm long) of the analysis cylinder within a particle. For the matrix, each data point represents the average from at least 9 sections (stacked histograms showing the Cu, Mg and Zn concentration in at.% of the matrix, GP zones and  $\eta'$  and  $\eta$  particles can be found for various specimens as Supplementary material). The results compare well with precipitate compositions from previous investigations, but there is a significant dispersion in the literature. The reason for the differences with some of the reported compositions [23,35] is that in these works the Al atoms of the matrix are removed. However, the relative amounts of Cu, Mg, and Zn in those works are close to our results if Al is not taken into account.

Surface densities and dimensions measured from SEM images are not presented because: 1) many small particles are probably overlooked due to the lower resolution of SEM; and 2) it is hard to assure whether the visible small particles are actually cut by the cutting face or they are just halos from particles in deeper layers, and it is not possible to discriminate whether they are GP zones or  $\eta'$  particles. Fig. 10 shows the dimensions of GP zones and  $\eta'$  particles measured from HRTEM and TEM images, respectively. Each data point represents the average from 50 to 150 measurements. The dimensions of GP zones obtained from APT and HRTEM are similar for specimen 2 (4.2 vs. 4.5 nm), but not for specimen 3 (4.6 vs. 8.7 nm). Also, the dimensions of  $\eta'$  particles from TEM appear larger than from APT. These discrepancies are due to the small size of the volumes analyzed with APT, and the fact that large particles are less frequent. Thus, the probability for the latter to be captured as a whole within an analysis volume is lower [36]. For this reason, and the fact that the dimensions obtained from HRTEM images are averages from a much larger number of particles (and thus have higher statistical validity), the GP zones volume fraction is computed using the average volume as estimated from HRTEM measurements combined with particle densities obtained from APT (densities were not computed from HRTEM/TEM images because the thickness of the samples is unknown). Thus, the GP zones volume fraction is  $2.29 \pm 0.42\%$  and  $7.79 \pm 0.17\%$  for specimens 2 and 3, respectively. The values of volume fraction, particle density, and dimensions

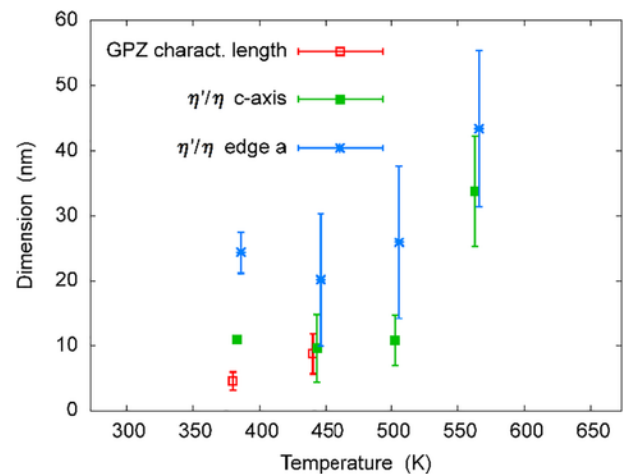


Fig. 10. GP zones characteristic length from HRTEM, and  $a$ -edge length and  $c$ -axis length of hexagonal  $\eta'/\eta$  cells from TEM, for AA 7075-T6 heated up to 383, 443, 503, 563 and 648 K (110, 170, 230, 290 and 375 °C). The  $a$ -edge length values show only the order of magnitude since the hexagonal faces are not seen in true scale. For clarity, points and error bars are slightly shifted artificially in the  $x$ -axis.

measured for the GP zones agree with the values in the literature [7,8,22].

The  $\eta'$  cell dimensions present a minimum for specimen 3. This is due to presence of primary  $\eta'$  particles in the as-received AA 7075-T6: for specimens 1 and 2, the averaged dimensions correspond basically to large, primary  $\eta'$  particles formed in the T6 temper, but for specimen 3 new (secondary)  $\eta'$  particles have formed, and these smaller particles cause a decrease in the averaged dimensions. The dimensions increase from specimen 3 to 4 due to the growth of both the primary and secondary  $\eta'$  particles. The  $\eta'/\eta$  phase volume fraction derived from the SEM images are particularly valuable (see Fig. 11) since there is no such data in the literature.

The small discrepancies between our results and previous works may be due to the fact that GP zones and  $\eta'$  particles are metastable, and thus their dimensions, chemical composition, and structure are sensitive to the solute content and heat-treatment conditions. Discrepancies in the APT results may also be due to differences in the test conditions, like the vacuum and base specimen temperature, or experimental errors or difficulties in correctly identifying the precipitates under analysis [6].

## 5. Modeling of the Viscoelastic Response

The experimental data reported in this work, and viscoelasticity measurements from previous dynamic-mechanical analysis [24,28,37], were used to test a model of the viscoelastic response of the Al-Zn-Mg-Cu alloy. In this approach, a reaction rate equation for formation and dissolution of GP zones and a reaction rate equation for  $\eta'$  phase formation were integrated numerically inside the least-squares nonlinear fitting of a model of the storage modulus,  $E'$ , i.e., the elastic (real) component of the dynamic tensile modulus, a measure of the deformation energy stored by the material during cyclic loading. This model (Eq. (6) in [24]) describes  $E'$  as a function of the loading frequency, temperature,  $T$ , GP zones volume fraction,  $C_1$ , and  $\eta'$  phase volume fraction,  $C_2$ . For the  $\eta'$  phase formation rate, the Avrami equation was used [38] (Eq. (8) in [24]), for which the key parameters are the Avrami index,  $n$ , and the characteristic transformation time,  $\tau$ , with  $1/\tau$  having Arrhenius-type temperature dependence, and thus having two associated kinetic parameters: a pre-exponential coefficient,  $k_0$ , and the activation energy,  $E_A$ . More details on this approach and the model can be found in [24] and as Supplementary material. A difference respect

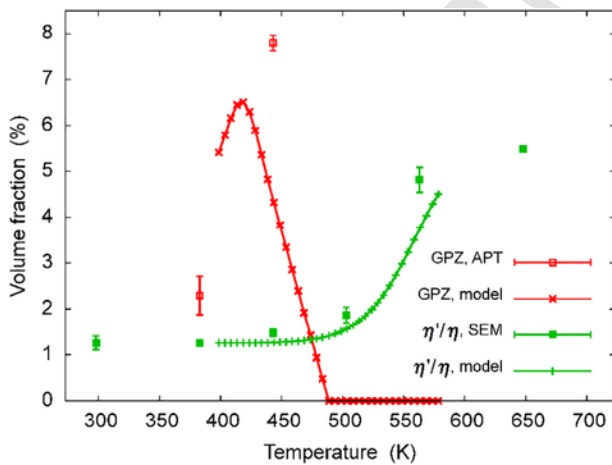


Fig. 11. GP zones volume fraction and  $\eta'/\eta$  phase volume fraction vs. temperature under continuous heating at a constant heating rate of  $\approx 1$  K/min. The GP zones volume fraction is obtained from APT and from a reaction rate model accounting for diffusion controlled growth (with soft impingement) [39] and redissolution. The  $\eta'/\eta$  phase volume fraction is obtained from SEM and from the Avrami equation [38].

to [24] is that, for the GP zones, the reaction rate model now accounts for two competing processes: diffusion controlled growth (with soft impingement) and redissolution. For the first mechanism, a model proposed in [39] is used, while the second process is modeled with a simple diffusion equation:

$$D_1(t) = D_{0,1} \exp\left(-\frac{E_{A,1}}{k_B T(t)}\right)$$

$$D_2(t) = D_{0,2} \exp\left(-\frac{E_{A,2}}{k_B T(t)}\right)$$

$$D_{eff}(t) = D_1(t) \left(1 - \frac{x(t)}{\gamma}\right) \frac{\gamma}{1 - x(t)} - D_2(t)$$

where  $D_1$  accounts for the diffusion of Mg contributing to growth of GP zones (at low temperature, the rate-limiting factor in a precipitation process in solid state is often the diffusion of the slowest solute species [2]; in this case, Mg, which was suggested as the limiting factor in GP-I zones formation [13]),  $D_{0,1}$  and  $E_{A,1}$  are respectively the pre-exponential coefficient and activation energy for Mg diffusion in Al,  $k_B$  is the Boltzmann constant,  $D_2$  accounts for an apparent diffusion contributing to dissolution of GP zones,  $D_{0,2}$  and  $E_{A,2}$  are respectively the pre-exponential coefficient and activation energy for this apparent diffusion,  $D_{eff}$  is the effective diffusion (positive when GP zones are growing and negative when GP zones are redissolving),  $x$  is the GP zones transformed fraction, and  $\gamma$  is the ratio between the average concentration of Mg in the alloy and the concentration of Mg in the GP zones (assumed constant). To compute  $x$ , expressions for growth from Zener [40], further collected by Christian [41], were used. Particularly, in 3D diffusion controlled growth with spherical symmetry, and in the steady regime, the position of the interface is given by:  $R = \alpha_3 \sqrt{Dt}$ , where  $R$  is the radius, and  $\alpha_3$  is a complex function of the concentration of the diffusing species inside the grain ( $r \rightarrow 0$ ) and far away from the grain ( $r \rightarrow \infty$ ). Thus,  $D_{eff}$  can be defined as  $D_{eff} = \alpha_3^2 D/2$ . Finally, the following expressions were used for the GPZ radius and  $x$ , assuming  $\alpha_3^2/2 \approx 1$ , which are very convenient for computing purposes:

$$\begin{aligned} (R_{GPZ}(t_{i+1}))^2 &= (R_{GPZ}(t_i))^2 + \alpha_3^2 D(t_i) \Delta t \\ &= (R_{GPZ}(t_i))^2 + 2D_{eff}(t_i) \Delta t \end{aligned}$$

$$x(t_{i+1}) = \frac{4}{3} \pi (R_{GPZ}(t_{i+1}))^3 d$$

where  $R_{GPZ}(t_i)$  is the GP zones radius in the instant  $t_i$ ,  $\Delta t = t_{i+1} - t_i$  is the time step, and  $d$  is the density of GP zones, assumed constant.

In the proposed approach, where the  $E'$  model is fitted to experimental  $E'$  data, the kinetic parameters treated as fitting parameters are, for the formation of  $\eta'$  phase,  $n$ ,  $k_0$  and  $E_A$ , and, for the formation and dissolution of GP zones,  $D_{0,2}$  and  $E_{A,2}$  ( $D_{0,1}$  and  $E_{A,1}$  are given constant values, as obtained from the literature). Thus, the proposed procedure provides the best fit kinetic parameters and consequently the best fit curves of precipitate volume fraction vs. temperature (or time). Table 5 presents the initial values used for the fitting, as well as the best fit kinetic parameters obtained after this process. A thorough discussion of the latter results with respect to values reported in the literature is provided in [24,37]. The initial values for  $R_{GPZ}(0)$  and  $d$  were guessed from the measurements at the temperature closest to RT, i.e., the measurements for specimen 2 ( $L = 4.2$  nm and  $d = 3.5 \times 10^6$  GP zones per  $\mu\text{m}^3$ , respectively). It is not necessary to provide an initial value for  $C_1$



**Table 5**

Initial values for non-fitting and fitting parameters and best-fit values for the latter, obtained after integration and fitting of the reaction rate equations and the storage modulus model, for AA 7075-T6.

Parameter	Initial value	Reference	Final value <sup>a</sup>	Observations
Pre-exp. coef., $D_{0,1}$	$3.2 \times 10^{-6} \text{ m}^2 \text{ s}^{-1}$	[42]	n/a	Not a fitting parameter
Activation energy, $E_{A,1}$	1.16 eV/atom	[42]	n/a	Not a fitting parameter
Pre-exp. coef., $D_{0,2}$	$5.5 \times 10^{-6} \text{ m}^2 \text{ s}^{-1}$	This work	$8.75 \times 10^{-5} \text{ s}^{-1}$	
Activation energy, $E_{A,2}$	1.21 eV/atom	[24]	1.29 eV/atom	Averaged from the literature
Ratio $\gamma$	$2.99/13.79 = 0.217$	This work	n/a	Not a fitting parameter
GP zones radius, $R_{GPZ}(0)$	1.5 nm	This work	n/a	Not a fitting parameter
Time step, $\Delta t$	1 s	This work	n/a	Not a fitting parameter
GP zones density, $d$	$3.0 \times 10^6 \text{ } \mu\text{m}^{-3}$	This work	n/a	Not a fitting parameter
Number of steps, $i_{\text{max}}$	14,000	This work	n/a	Not a fitting parameter
Pre-exp. coef., $k_0$	$8.8 \times 10^9 \text{ s}^{-1}$	[24]	$8.99 \times 10^9 \text{ s}^{-1}$	
Activation energy, $E_A$	1.26 eV/atom	[24]	1.26 eV/atom	
Avrami index, $n$	0.85	[24]	0.66	
$\eta'$ phase vol. fraction, $C_2$	1.25%	This work	5.15%	Not a fitting parameter

<sup>a</sup> For non-fitting parameters that remain constant during the proposed procedure, this column displays “non-applicable” (n/a). For the fitting and non-fitting parameters that change during the integration and fitting procedure, this column displays the final value of the corresponding parameter at the end of the process.

since it is derived directly from  $R_{GPZ}(0)$  and  $d$ . The initial value for  $C_2$  corresponds to the  $\eta'$  phase volume fraction measured for specimen 1. Finally, the variation of  $C_2$  must be smaller than the  $\eta'/\eta$  phase volume fraction measured for specimen 6 minus the initial value for  $C_2$  (see also Supplementary material).

In Fig. 11, the GP zones volume fraction obtained from APT and the  $\eta'/\eta$  phase volume fraction estimated from SEM images are compared with model results obtained following the procedure described above. The model gives a satisfactory description of the volume fractions (especially for the  $\eta'/\eta$  phase), and also of the  $E'$  measured experimentally (see Supplementary material). As expected, the model results for  $\eta'$  phase are slightly below the measured volume fraction for specimens 5 and 6. This is mainly because the latter correspond to combined  $\eta'$  and  $\eta$  phase volume fractions, so they establish a threshold that the  $\eta'$  phase volume fraction given by the model cannot exceed. The conclusions that can be drawn for the GP zones are limited for several reasons: 1) there are only a couple of experimental values of volume fraction, obtained from a relatively low number of successful atom probe tests; and 2) the effect of the GP zones on the viscoelastic response of the alloys, if any, appears to be of a much lower magnitude than the effect of the  $\eta'$  phase. Thus, considering the resolution of the proposed approach, the error in the model results for the GP zones volume fraction is likely much more significant than for the  $\eta'$  phase.

## 6. Conclusions

A FIB-SEM, TEM, HRTEM, and APT analysis is performed to characterize the evolution of the microstructure of AA 7075-T6 (Al–Zn–Mg–Cu alloy) under continuous heating over the temperature range of 298 to 648 K (25 to 375 °C). The results illustrate the aging path of this family of alloys, and particularly the evolution of GP zones and  $\eta'$  and  $\eta$  phase. The chemical composition, dimensions, number density, and volume fraction of precipitates are measured comprehensively. The main conclusions from this research are:

- The total precipitate solute content increases from GP zones to  $\eta'$  phase, and from the latter to  $\eta$  phase.
- Spherical and ellipsoidal GP-I zones are identified, with an average characteristic length growing with temperature from 4.5 at 383 K (110 °C) to 8.7 nm at 443 K (170 °C), as obtained from HRTEM (from 4.2 to 4.6 nm, as obtained from APT).
- The average  $a$ -edge length of the hexagonal cells ( $\eta'/\eta$  phase) ranged from 24 to 43 nm, while the  $c$ -axis length ranged from 10 to 34 nm. These dimensions measured from HRTEM for some specimen types are larger than most results in the literature.

- The dimensions of the hexagonal cells with temperature show a minimum in the samples heated up to 443 K (170 °C). The minimum is due to averaging the dimensions of large, primary  $\eta'$  particles inherited from the as-received AA 7075-T6 with those of small, secondary  $\eta'$  particles formed during heating up to 443 K (170 °C).
- Number densities are above  $10^6$  GP zones per  $\mu\text{m}^3$  and  $5 \times 10^5$   $\eta'$  particles per  $\mu\text{m}^3$ .
- The volume fraction of GP zones (ranging from 2.3 to 7.8%) and  $\eta'/\eta$  phase (ranging from 1.3 to 5.5%) compare well with results in the literature.
- The good agreement between the model results and the test data suggests that variations in the viscoelastic behavior of Al–Zn–Mg alloy may be associated with the formation and dissolution of GP zones and  $\eta'$  phase formation.

## Acknowledgements

Work supported by the Spanish MINECO [grant number FIS2014-54734-P], the Generalitat de Catalunya/AGAUR [grant number 2014 SGR 581], and the Australian Research Council [grant number DP120100510]. The authors acknowledge the facilities as well as scientific and technical assistance from staff in the Australian Microscopy & Microanalysis Research Facility at the Australian Centre for Microscopy & Microanalysis (ACMM), The University of Sydney. The authors thank the valuable help and feedback from Prof. X. Liao, Prof. G. Sha, Mr. A. Sikorski, Dr. H.W. Liu, Dr. H.W. Yen, Dr. I. Poon, and Dr. T. Sato, of ACMM, and Dr. T. Todorov, of the Center for Research in NanoEngineering (CrnE), Universitat Politècnica de Catalunya.

## Conflicts of Interest

None.

## Appendix A. Supplementary Data

Supplementary data to this article can be found online at <https://doi.org/10.1016/j.matchar.2017.11.018>.

## References

- [1] E.A. Starke, J.T. Staley, Application of modern aluminum alloys to aircraft, Prog. Aerosp. Sci. 32 (1996) 131–172.
- [2] R. Ferragut, A. Somoza, A. Dupasquier, On the two-step ageing of a commercial Al–Zn–Mg alloy; a study by positron lifetime spectroscopy, J. Physics-Condensed Matter. 8 (1996) 8945–8952.

- [3] S.P. Ringer, K. Hono, Microstructural evolution and age hardening in aluminium alloys: atom probe field-ion microscopy and transmission electron microscopy studies, *Mater. Charact.* 44 (2000) 101–131.
- [4] T. Engdahl, V. Hansen, P.J. Warren, K. Stiller, Investigation of fine scale precipitates in Al–Zn–Mg alloys after various heat treatments, *Mater. Sci. Eng. A-Struct. Mater. Prop. Microstruct. Process.* 327 (2002) 59–64.
- [5] F. Viana, A.M.P. Pinto, H.M.C. Santos, A.B. Lopes, Retrogression and re-ageing of 7075 aluminium alloy: microstructural characterization, *J. Mater. Process. Technol.* 93 (1999) 54–59.
- [6] S.K. Maloney, K. Hono, I.J. Polmear, S.P. Ringer, The chemistry of precipitates in an aged Al–2.1Zn–1.7Mg at.% alloy, *Scr. Mater.* 41 (1999) 1031–1038, [https://doi.org/10.1016/S1359-6462\(99\)00253-5](https://doi.org/10.1016/S1359-6462(99)00253-5).
- [7] S.S. Singh, J.J. Loza, A.P. Merkle, N. Chawla, Three dimensional microstructural characterization of nanoscale precipitates in AA7075-T651 by focused ion beam (FIB) tomography, *Mater. Charact.* 118 (2016) 102–111, <https://doi.org/10.1016/j.matchar.2016.05.009>.
- [8] C. Schmuck, P. Auger, F. Danoix, D. Blavette, Quantitative analysis of GP zones formed at room-temperature in a 7150-Al-based alloy, *Appl. Surf. Sci.* 87–8 (1995) 228–233, [https://doi.org/10.1016/0169-4332\(94\)00501-X](https://doi.org/10.1016/0169-4332(94)00501-X).
- [9] A. Bigot, F. Danoix, P. Auger, D. Blavette, A. Reeves, Tomographic atom probe study of age hardening precipitation in industrial AlZnMgCu(7050) alloy, *Mater. Sci. Forum* 217 (1996) 695–700.
- [10] X.M. Li, M.J. Starink, Effect of compositional variations on characteristics of coarse intermetallic particles in overaged 7000 aluminium alloys, *Mater. Sci. Technol.* 17 (2001) 1324–1328.
- [11] V. Hansen, K. Stiller, G. Waterloo, J. Gjønnes, X.Z. Li, Structures and transformations during artificial aging of an industrial 7xxx-series Al–Zn–Mg–Zr alloy, *Mater. Sci. Forum* 396–402 (2002) 815–820.
- [12] S.R. Ortner, C.R.M. Grovenor, B.A. Shollock, On the structure and composition of GP zones in high-purity AlZnMg alloys, *Scr. Metall.* 22 (1988) 839–842, [https://doi.org/10.1016/S0036-9748\(88\)80060-7](https://doi.org/10.1016/S0036-9748(88)80060-7).
- [13] G. Sha, A. Cerezo, Early-stage precipitation in Al–Zn–Mg–Cu alloy (7050), *Acta Mater.* 52 (2004) 4503–4516, <https://doi.org/10.1016/j.actamat.2004.06.025>.
- [14] N.Q. Chinh, J. Lendvai, D.H. Ping, K. Hono, The effect of Cu on mechanical and precipitation properties of Al–Zn–Mg alloys, *J. Alloys Compd.* 378 (2004) 52–60, <https://doi.org/10.1016/j.jallcom.2003.11.175>.
- [15] K. Hono, N. Sano, T. Sakurai, Quantitative atom-probe analysis of some aluminium-alloys, *Surf. Sci.* 266 (1992) 350–357, [https://doi.org/10.1016/0039-6028\(92\)91045-D](https://doi.org/10.1016/0039-6028(92)91045-D).
- [16] U. Batra, S.R. Prabhakar, Differential scanning calorimetric analysis for 7075-aluminium-alloy, *Trans. Indian Inst. Metals* 48 (1995) 55–61.
- [17] C.E. Lyman, J.B. Vandersande, Transmission electron-microscopy investigation of early stages of precipitation in an Al–Zn–Mg alloy, *Metall. Trans. A-Phys. Metall. Mater. Sci.* 7 (1976) 1211–1216.
- [18] K. Stiller, P.J. Warren, V. Hansen, J. Angenete, J. Gjønnes, Investigation of precipitation in an Al–Zn–Mg alloy after two-step ageing treatment at 100 degrees and 150 degrees C, *Mater. Sci. Eng. A-Struct. Mater. Prop. Microstruct. Process.* 270 (1999) 55–63.
- [19] M.M. Sharma, M.F. Amateaub, T.J. Eden, Hardening mechanisms of spray formed Al–Zn–Mg–Cu alloys with scandium and other elemental additions, *J. Alloys Compd.* 416 (2006) 135–142.
- [20] X.Z. Li, V. Hansen, J. Gjønnes, L.R. Wallenberg, HREM study and structure modeling of the  $\epsilon'$  phase, the hardening precipitates in commercial Al–Zn–Mg alloys, *Acta Mater.* 47 (1999) 2651–2659.
- [21] G. Sha, A. Cerezo, Kinetic Monte Carlo simulation of clustering in an Al–Zn–Mg–Cu alloy (7050), *Acta Mater.* 53 (2005) 907–917, <https://doi.org/10.1016/j.actamat.2004.10.048>.
- [22] A. Deschamps, F. De Geuser, Z. Horita, S. Lee, G. Renou, Precipitation kinetics in a severely plastically deformed 7075 aluminium alloy, *Acta Mater.* 66 (2014) <https://doi.org/10.1016/j.actamat.2013.11.071>.
- [23] G. Sha, Y.B. Wang, X.Z. Liao, Z.C. Duan, S.P. Ringer, T.G. Langdon, Influence of equal-channel angular pressing on precipitation in an Al–Zn–Mg–Cu alloy, *Acta Mater.* 57 (2009) 3123–3132, <https://doi.org/10.1016/j.actamat.2009.03.017>.
- [24] J.I. Rojas, D. Crespo, Modeling of the effect of temperature, frequency and phase transformations on the viscoelastic properties of AA 7075-T6 and AA 2024-T3 aluminium alloys, *Metall. Mater. Trans. A.* 43 (2012) 4633–4646, <https://doi.org/10.1007/s11661-012-1281-7>.
- [25] G. Sha, R.K.W. Marceau, X. Gao, B.C. Muddle, S.P. Ringer, Nanostructure of aluminium alloy 2024: segregation, clustering and precipitation processes, *Acta Mater.* 59 (2011) 1659–1670, <https://doi.org/10.1016/j.actamat.2010.11.033>.
- [26] B. Gault, M.P. Moody, F. de Geuser, G. Tsafnat, A. La Fontaine, L.T. Stephenson, D. Haley, S.P. Ringer, Advances in the calibration of atom probe tomographic reconstruction, *J. Appl. Phys.* 105 (2009) 34913, <https://doi.org/10.1063/1.3068197>.
- [27] S. Pogatscher, H. Antrekowitsch, H. Leitner, T. Ebner, P.J. Uggowitzer, Mechanisms controlling the artificial aging of Al–Mg–Si alloys, *Acta Mater.* 59 (2011) 3352–3363, <https://doi.org/10.1016/j.actamat.2011.02.010>.
- [28] J.I. Rojas, A. Aguiar, D. Crespo, Effect of temperature and frequency of dynamic loading in the viscoelastic properties of aluminium alloy 7075-T6, *Phys. Status Solidi C* 8 (2011) 3111–3114, <https://doi.org/10.1002/pssc.201000732>.
- [29] E.S. Tankins, W.E. Frazier, Differential scanning calorimetric studies of the corrosion-resistant behavior in the 7000 series aluminum-alloys, *Mater. Perform.* 26 (1987) 37–44.
- [30] E. Thompson, Quantitative microscopic analysis, *J. Geol.* 38 (1930) 193.
- [31] C. Mondal, A.K. Mukhopadhyay, On the nature of T(Al<sub>2</sub>Mg<sub>3</sub>Zn<sub>3</sub>) and S(Al<sub>2</sub>CuMg) phases present in as-cast and annealed 7055 aluminum alloy, *Mater. Sci. Eng. A-Struct. Mater. Prop. Microstruct. Process.* 391 (2005) 367–376, <https://doi.org/10.1016/j.msea.2004.09.013>.
- [32] A. Bigot, P. Auger, S. Chambrelaud, D. Blavette, A. Reeves, Atomic scale imaging and analysis of T' precipitates in Al–Mg–Zn alloys, *Microsc. Microanal. Microstruct.* 8 (1997) 103–113, <https://doi.org/10.1051/mm:1997109>.
- [33] J.M. Papazian, Calorimetric studies of precipitation and dissolution kinetics in aluminium-alloys 2219 and 7075, *Metall. Trans. A-Phys. Metall. Mater. Sci.* 13 (1982) 761–769.
- [34] E. Salamci, Calorimetric and transmission electron microscopy studies of spray deposited Al–Zn–Mg–Cu alloys, *Mater. Sci. Technol.* 20 (2004) 859–863, <https://doi.org/10.1179/026708304225010433>, (ER).
- [35] W. Lefebvre, F. Danoix, G. Da Costa, F. De Geuser, H. Hallern, A. Deschamps, M. Dumont, 3DAP measurements of Al content in different types of precipitates in aluminium alloys, *Surf. Interface Anal.* 39 (2007) 206–212, <https://doi.org/10.1002/sia.2516>.
- [36] G. Sha, A. Cerezo, Characterization of precipitates in an aged 7xxx series Al alloy, *Surf. Interface Anal.* 36 (2004) 564–568, <https://doi.org/10.1002/sia.1702>.
- [37] J.I. Rojas, J. Nicolás, D. Crespo, Study on mechanical relaxations of 7075 (Al–Zn–Mg) and 2024 (Al–Cu–Mg) alloys by application of the time-temperature superposition principle, *Adv. Mater. Sci. Eng.* 2017 (2017) 1–12, <https://doi.org/10.1155/2017/2602953>.
- [38] M.J. Starink, A.M. Zahra, An analysis method for nucleation and growth controlled reactions at constant heating rate, *Thermochim. Acta* 292 (1997) 159–168.
- [39] M.T. Clavaguera-Mora, N. Clavaguera, D. Crespo, T. Pradell, Crystallisation Kinetics and Microstructure Development in Metallic Systems, 2002.
- [40] C. Zener, Theory of growth of spherical particles, *J. Appl. Phys.* 20 (1949) 950–953.
- [41] J.W. Christian, *The Theory of Transformations in Metals and Alloys*, Pergamon, Oxford, UK, 2002.
- [42] J. Xin, W. Zhang, J. Wang, D. Zhao, Y. Du, L. Zhang, B. Huang, Prediction of diffusivities in fcc phase of the Al–Cu–Mg system: first-principles calculations coupled with CALPHAD technique, *Comput. Mater. Sci.* 90 (2014) 32–43, <https://doi.org/10.1016/j.commatsci.2014.03.057>.